




Strengthening of the f mode due to subsurface magnetic fields in simulations of convectionG. KISHORE ¹, NISHANT K SINGH ¹, PETRI KÄPYLÄ ², AND MARKUS ROTH³¹*IUCAA, Post Bag 4, Ganeshkhind, Pune 411007, India*²*Institut für Sonnenphysik (KIS), Georges-Köhler-Allee 401a, 79110 Freiburg im Breisgau, Germany*³*Thüringer Landessternwarte Tautenburg and Friedrich-Schiller-Universität Jena, Germany*

ABSTRACT

Previous studies have found that localized strengthening of the f mode precedes the emergence of active regions on the Sun by one day to three days. To help interpret these observations, we have performed nonlinear simulations of convection with imposed magnetic fields at different depths. We find that the f mode is strengthened when a super-equipartition magnetic field is imposed near the top of the domain. However, neither a magnetic field of equal strength near the bottom of the domain nor an equipartition magnetic field near the top of the domain have a significant effect. Our results suggest that the magnetic precursors of active regions are present near the surface of the Sun for much longer than would be expected if active regions were formed by flux tubes rising from deep within the convection zone. Application to observations should account for the fact that the effects we observe are transient.

Keywords: Helioseismology (709), Solar magnetic fields (1503), Solar convective zone (1998)

1. INTRODUCTION

The Sun supports a wide variety of waves. Depending on the nature of the restoring force, the corresponding modes (Leibacher & Stein 1981) are classified into various branches. The eigenfunctions of each type of mode have characteristic dependences on depth, and are thus sensitive to different layers of the Sun. Helioseismology uses observations of the amplitudes and frequencies of these modes at the solar surface to infer the properties of deeper layers (Christensen-Dalsgaard 2002; Thompson 2006).

At a free surface, the incompressible deep-water equations support horizontally travelling waves whose ampli-

tudes decay exponentially with depth over a scale proportional to their wavelength (e.g. Acheson 1990, sec. 3.2 and exercise 3.2). These waves are also supported at interfaces with a finite density contrast. In the stellar context, the associated modes are usually referred to as f (fundamental) modes. Since their eigenfunctions decay rapidly with depth (at least for large horizontal wavenumbers), these modes are only expected to be affected by the near-surface layers of the star.

Singh et al. (2016) and Waidele et al. (2023a) have found that localized strengthening of the solar f mode precedes the emergence of an active region by one day to three days.¹ For the large horizontal wavenumbers considered in these observations, the eigenfunction of the f mode is expected to decay with depth over a scale of a few Mm. For example, Singh et al. (2016) considered f modes with $kR_{\odot} > 1200$, which decay over less than 0.6 Mm. This suggests that the precursors of

Corresponding author: G. Kishore

kishore@iucaa.in

nishant@iucaa.in

pkapyla@leibniz-kis.de

mroth@tls-tautenburg.de

¹Korpi-Lagg et al. (2022), on the other hand, find that there is no significant effect. Appendix D discusses a possible reason for this disagreement.

active regions can be present in the upper few Mm of the convection zone (CZ) up to three days before their emergence.

Sunspot formation is often explained by appealing to magnetic flux tubes buried at the bottom of the CZ, approximately 200 Mm below the surface (for a review, see Charbonneau 2020). Such flux tubes may rise either due to magnetic buoyancy (Parker 1975), or due to kink instabilities (Babcock 1961, p. 577). Rising flux tubes are expected to cross the top 10 Mm of the CZ (around 11 pressure scale heights) in a few hours (Cheung et al. 2010). This is difficult to reconcile with the aforementioned observations.

Going beyond the qualitative reasoning described above, one would like to use mode amplitudes to quantitatively constrain the locations, strengths, and configurations of subsurface magnetic fields. However, analytical predictions of the effects of magnetic fields on helioseismic modes typically only consider simple magnetic field configurations, and are limited to studying frequency shifts (e.g. Miles et al. 1992; Tripathi & Mitra 2022; Rui & Fuller 2023). The general formalism presented by Kiefer et al. (2017) and Kiefer & Roth (2018) also only deals with frequency shifts.

Singh et al. (2014, 2015, 2020) performed 2D simulations where turbulence is driven by a prescribed forcing function in a piecewise isothermal background. Imposing magnetic fields of different configurations, they observed changes in the frequencies and the amplitudes of various modes. Singh et al. (2015, sec. 4.2) found that a strong, uniform, horizontal magnetic field suppresses the amplitude of the f mode at all wavenumbers. In their setup, they found that the mode amplitude is correlated with the RMS velocity of the flow; it is only through the latter that the magnetic field affects the mode amplitudes. On the other hand, Singh et al. (2020, sec. 3.3) found that when the magnetic field is localized, the f mode is strengthened at large wavenumbers, but only when the magnetic field is near the surface.

The amplitude of a particular mode depends on the spectral properties of the forcing function used (Batchelor 1953, sec. 4.1; Christensen-Dalsgaard 2002, sec. V.F). In the case of the Sun, the modes are excited by convective flows, which may themselves be affected by the presence of a magnetic field. Thus, while the analytical studies and idealized forced-turbulence simulations described above can be used to understand how the frequencies of various modes are affected by magnetic fields, it is unclear if their findings on the amplitudes of various modes can be applied to convective systems. The amplitudes are sensitive to the nature of the fluid flows, and so one has to perform nonlinear simulations

of stratified convection to capture the relevant effects. While many authors have observed modes (f, p, and Rossby) in simulations of convection (e.g. Zhao et al. 2007; Bekki et al. 2022; Waidele et al. 2023b; Blume et al. 2024), we are not aware of any studies of magnetic effects on modes in such simulations.

In this study, we use simulations in which convection is driven by a prescribed cooling function at the top of the domain. Peaks of the horizontally and temporally Fourier-transformed vertical velocity from such simulations can be associated with f, p, and g modes. Imposing horizontal magnetic fields localized at different depths, we probe their effects on the amplitude of the f mode near the top of the domain.

In section 2, we specify our simulation setup. Section 3 defines quantities in terms of which we report our results. Section 4 describes the statistically steady state of our non-magnetic simulation. In section 5, we report the effects of imposed magnetic fields on the f mode. We summarize our work in section 6.

2. NUMERICAL SETUP

2.1. Domain and evolution equations

We consider a Cartesian domain, periodic in the x and y directions. Gravity points along the $-\hat{z}$ direction. The domain extends vertically between $-0.45l < z < 1.05l$, where l is the depth of the initially unstable region.

We solve the following evolution equations:

$$\frac{D \ln \rho}{dt} = -\nabla \cdot \mathbf{u} \quad (1)$$

$$\rho \frac{D\mathbf{u}}{dt} = -\nabla p - \rho g \hat{z} + \mathbf{J} \times \mathbf{B} + \nabla \cdot (2\rho\nu \overleftrightarrow{S}) \quad (2)$$

$$\rho T \frac{Ds}{dt} = q - \nabla \cdot (\mathbf{F}_{\text{rad}} + \mathbf{F}_{\text{SGS}}) + 2\rho\nu S_{ij} S_{ij} \quad (3)$$

where

$$\mathbf{B} \equiv \nabla \times \mathbf{A} \quad (4)$$

$$\mathbf{J} \equiv \frac{\nabla \times \mathbf{B}}{\mu_0} \quad (5)$$

$$S_{ij} \equiv \frac{1}{2} \left(\partial_i u_j + \partial_j u_i - \frac{2}{3} \delta_{ij} \nabla \cdot \mathbf{u} \right) \quad (6)$$

with ρ being the density; \mathbf{u} the velocity; $D/dt \equiv \partial/\partial t + \mathbf{u} \cdot \nabla$ the convective derivative; p the pressure; g the acceleration due to gravity (with $g > 0$); ν the kinematic viscosity; s the specific entropy; \mathbf{A} the magnetic vector potential; and μ_0 the magnetic permeability. A similar setup (without magnetic fields) has been used by Käpylä (2019, 2021).

We choose units such that $g = C_P = l = \rho_0 = 1$, where C_P is the specific heat at constant pressure, and

ρ_0 is the initial density at the top of the domain. With these choices, the unit for length is l ; mass is $\rho_0 l^3$; time is $\sqrt{l/g}$; temperature is gl/C_P ; and magnetic field is $\sqrt{\mu_0 \rho_0 gl}$. We assume the kinematic viscosity is a constant ($\nu = 10^{-4} l^{3/2} g^{1/2}$), and neglect the bulk viscosity (omitted from the expressions above).

In the evolution equation for the entropy, \mathbf{F}_{rad} is the radiative flux determined by the Kramers opacity formula (i.e. the thermal conductivity is itself a function of the temperature and the density), such that

$$\mathbf{F}_{\text{rad}} = -K_0 \rho^{-2} T^{13/2} \nabla T \quad (7)$$

where T is the temperature. Käpylä et al. (2017) have studied how such a prescription differs from more common choices. We set $K_0 \approx 1.41 \rho_0^3 C_P^{15/2} l^{-5} g^{-6}$.

Following Käpylä (2021), for numerical reasons, we also add a subgrid-scale (SGS) diffusivity that acts on the fluctuations of the entropy about its horizontal average. The SGS diffusivity is set to $\chi_{\text{SGS}} = 10^{-4} l^{3/2} g^{1/2}$, and the entropy flux due to it is given by

$$\mathbf{F}_{\text{SGS}} \equiv -\rho T \chi_{\text{SGS}} \nabla s', \quad s' \equiv s - \langle s \rangle_{xy}. \quad (8)$$

A cooling function, q , of the form

$$q = -\frac{\rho (c_s^2 - c_{\text{cool}}^2)}{\tau_{\text{cool}}} \Theta \left(\frac{z - z_{\text{cool}}}{w_{\text{cool}}} \right) \quad (9)$$

with $\Theta(z) \equiv (1 + \text{erf}(z))/2$, $z_{\text{cool}} = l$, $c_{\text{cool}}^2 = 0.09 gl$, $w_{\text{cool}} = 0.025 l$, and $\tau_{\text{cool}} = (1/27) \sqrt{l/g}$ is also added to the entropy equation. This forces the adiabatic sound speed (c_s) in $z > z_{\text{cool}}$ to c_{cool} over a timescale τ_{cool} .

The fluid is chosen to be an ideal gas, whose equation of state is

$$p = \rho RT = \rho_0 RT_0 \left(\frac{\rho}{\rho_0} \right)^\gamma e^{\gamma s/C_P} \quad (10)$$

where $R \equiv C_P - C_V$ and $\gamma \equiv C_P/C_V$, with C_V being the specific heat at constant volume. We set $\gamma = 5/3$, corresponding to a monoatomic gas. Note that the zero point of the entropy is determined by the constant T_0 , which we choose such that $(\gamma - 1) C_P T_0 = c_{\text{cool}}^2$.

We prescribe a time-independent magnetic field by choosing the following form for \mathbf{A} :

$$A_y = \begin{cases} \frac{2C}{\pi} (z_2 - z_1) & z < z_1 \\ \frac{C}{\pi} (z_2 - z_1) \left(1 + \cos \left[\pi \frac{z - z_1}{z_2 - z_1} \right] \right) & z_1 \leq z < z_2 \\ 0 & z_2 \leq z \end{cases} \quad (11)$$

with $A_x = A_z = 0$. This is constructed in such a way that the resultant magnetic field is in the \hat{x} direction,

is a function of only z , and is localized in the region $z_1 < z < z_2$. C is the maximal value of the magnetic field. Table 1 gives the values of C , z_1 , and z_2 for all the simulations we consider, while the resulting profiles of B_x are plotted in figure 3.

These evolution equations are solved using the Pencil code (Pencil Code Collaboration et al. 2021).² Spatial derivatives are discretized using a sixth-order finite difference scheme, while the equations are evolved in time using a third-order Runge-Kutta method. Upwinding is used for advection of the density, the velocity, and the entropy. We use $N_x \times N_y \times N_z = 1152^2 \times 288$ grid points with $L_x = L_y = 16l$. In appendix A, we show that the convective flows are well-resolved with the chosen grid spacing.

2.2. Boundary conditions

The vertical boundaries are made free-slip, impenetrable, and perfect electric conductors. The total energy flux at the bottom is constrained to be $F_{\text{bot}} \equiv 5 \times 10^{-4} \rho_0 g^{3/2} l^{3/2}$, while the temperature at the top is constrained to be T_0 .

2.3. Initial conditions

To have decent resolution in k -space, we require the aspect ratio (horizontal/vertical dimension) of the domain to be large. However, running such simulations till they reach a statistically steady state is expensive. While an accelerated evolution scheme has been proposed to reduce the amount of time required to reach steady state (Anders et al. 2018), implementing it in an existing code seems complicated. We use a different approach, described below.

We first run a non-magnetic simulation with $L_x = L_y = l$ for $10^4 \sqrt{l/g}$ time units. For this simulation, the initial condition is piecewise polytropic, with the polytropic index being given by

$$\begin{cases} 3.25 & z < 0, \\ 1.5 & 0 < z < l, \\ \infty & l < z. \end{cases} \quad (12)$$

The temperature at the top is set to T_0 . The velocity at each grid point is randomly chosen such that each of its components are uniformly distributed between $\pm 10^{-4} \sqrt{gl}$.

A snapshot (an array containing all the state variables at each grid point) from this simulation is then periodically tiled to generate the initial condition for the non-magnetic simulation. To break the symmetry

² <https://pencil-code.nordita.org>

Name	C [$\sqrt{\mu_0 \rho_0 g l}$]	z_1 [l]	z_2 [l]	Time range [$\sqrt{l/g}$]	Realizations	Ra_{SGS} [10^6]	Re	Ra [10^7]	Nu	Ma_{max}	Ra_F [10^8]	Comment
NF	0			300–1300	4	1.6	265	7.5	15	0.12	4.6	No Field
ST	0.5	0.4	1.05	0–250	8	2.7	373	13	13	0.16	5.2	Strong Top
ST	0.5	0.4	1.05	250–500	8	1.9	336	9.5	14	0.15	5.2	Strong Top
SB	0.5	−0.45	0.2	0–250	6	1.6	268	7.5	15	0.12	4.7	Strong Bottom
ET	0.14	0.4	1.05	0–250	6	1.6	273	7.6	14	0.13	4.6	Equipartition Top

Table 1. Summary of the discussed simulations, along with diagnostics computed from a single realization of each configuration. For the magnetic cases, $t = 0$ corresponds to the time when the magnetic field is imposed. The diagnostics have been computed by averaging over the entire interval indicated. The same interval was used to compute the power spectra. Recall that for all the runs, $\nu = \chi_{SGS}$.

of the initial condition, low-amplitude grid-scale noise (with each of its components at each grid point uniformly distributed between $\pm 10^{-3} \sqrt{gl}$) is added to the velocity field. This leads to the symmetry of the initial condition being broken within a few turnover times. We produce four realizations of the non-magnetic case, differing only in the initial random component of the velocity field added during tiling. For all our analyses, we ignore data from the first 300 $\sqrt{l/g}$ time units of the larger non-magnetic simulations.

The magnetic simulations are initialized from snapshots of the non-magnetic simulations. To ensure statistical independence of the different realizations of a particular magnetic configuration, we ensure that even when two such realizations are initialized from the same non-magnetic realization, the snapshots have a minimum time-separation of 1000 $\sqrt{l/g}$.

2.4. Simulation output

The horizontal Fourier transform of the vertical component of the velocity is saved at all depths for $|k_x|, |k_y| \leq \gamma g / c_{top}^2$ at intervals of 0.1 $\sqrt{l/g}$ time units (0.5 $\sqrt{l/g}$ for the non-magnetic case). The temporal Fourier transform is later performed during post-processing.

2.5. Sources of error

We expect the two main sources of error to be (i) the finiteness of the integration time; and (ii) the spatial discretization used. We estimate the error due to the former by considering multiple realizations of the same configuration. Appendix A studies how the spatial discretization affects the results of this study.

Unless otherwise mentioned, realization-dependent quantities are estimated by averaging over all realizations; we consider the error in this estimate to be σ / \sqrt{N} , where σ is the standard deviation between different realizations and N is the number of realizations. Note that an estimate of this kind does not account for the error due to the spatial discretization.

3. DEFINITIONS, CONVENTIONS, AND MODELS

3.1. Dimensional scales

As the length and frequency scales, we take

$$L_0 \equiv \frac{c_{top}^2}{\gamma g}, \quad \omega_0 \equiv \frac{g}{c_{top}}. \quad (13)$$

Note that L_0 would be the pressure scale height at the top of the domain if it were in hydrostatic equilibrium; ω_0 is proportional to the acoustic cutoff frequency in an isothermal background.

Using these, we define dimensionless wavenumbers and frequencies as

$$\tilde{\omega} \equiv \frac{\omega}{\omega_0}, \quad \tilde{k}_i \equiv k_i L_0. \quad (14)$$

3.2. Power spectrum

Defining $\tilde{u}(\omega, k_x, k_y, z)$ as the discrete Fourier transform³ of $u_z(t, x, y, z)$ in time and the two horizontal directions, we define the power as

$$P(\tilde{\omega}, \tilde{k}_x, \tilde{k}_y, z) \equiv |\tilde{u}(\omega, k_x, k_y, z)|^2. \quad (15)$$

Previous studies (Singh et al. 2014, eq. 5; Singh et al. 2015, eq. 12; Singh et al. 2020, eq. 8) used the absolute value of the Fourier-transformed velocity, rather than its square. Our choice has been used in observational studies (e.g. Singh et al. 2016, p. 2). Note that it is the squared magnitude of the Fourier transform that is expected to show a Lorentzian mode profile (Batchelor 1953, sec. 4.1; Christensen-Dalsgaard 2002, sec. V.F).

3.3. Fitting modes

Consider the power spectrum, defined in equation 15, at fixed \tilde{k}_x , \tilde{k}_y , and z . We model it as the sum of a

³ For a periodic function, $f(x)$, defined on $-L/2 \leq x < L/2$, we use the convention that its Fourier transform, f_n , is given by $\frac{1}{L} \int_{-L/2}^{L/2} f(x) e^{-2\pi i n x / L} dx$.

power-law (the continuum) and a number of Lorentzians (each corresponding to a mode). For nonlinear least-squares fitting, we use an implementation of a trust-region reflective algorithm, provided by SciPy (Virtanen et al. 2020). The errors in $P(\tilde{\omega})$ (estimated as described in section 2.5) are propagated in the usual way to estimate errors in the fit parameters. Appendix C gives more details on these steps.

3.4. Mode mass

Given a particular mode, if the resolution in ω is not much smaller than the width of that mode, the peak value of $\tilde{u}(\omega)$ is sensitive both to the resolution and to any additional smoothing kernels that one may employ. As a measure of the strength of a particular mode, Singh et al. (2015, eq. 19) defined a ‘mode mass’, which is proportional to $\int \Delta\tilde{u} d\omega$, where $\Delta\tilde{u}$ denotes \tilde{u} after removal of a ‘continuum’ (and possibly other modes of disinterest).

We define the mode mass as

$$\mu \equiv \sum_{\tilde{\omega}} \Delta P(\tilde{\omega}) \quad (16)$$

where $\Delta P(\tilde{\omega})$ is the component corresponding to the mode of interest in the fit to the power spectrum (section 3.3). By virtue of Parseval’s theorem (Bracewell 2000, problem 10.24), μ defined in this way measures the temporally averaged specific kinetic energy associated with a particular mode; it is independent of the integration time if the system is in a statistically steady state. The analogous quantities defined by Singh et al. (2015, eq. 19) and Singh et al. (2020, eq. 9) do not have this property.^{4,5}

The errors in the fit parameters (section 3.3) are used to estimate the error in the mode mass by computing the mode mass for 10^4 realizations of the fit parameters (assumed to be normally distributed, with the distribution truncated at zero for parameters which are expected to be non-negative). The upper and lower errors in the mode mass are then estimated from the 84.1 and 15.9 percentile values of the mode mass (these correspond to $1\text{-}\sigma$ deviates for a normal distribution).

3.5. Fluxes

The averaged total energy density (kinetic + internal + gravitational) is transported by the following fluxes:

$$\mathbf{F}_{\text{enth}} \equiv \langle \rho C_P \mathbf{u} T \rangle_{xyt} \quad (17)$$

⁴ Singh et al. (2020, p. 207) allude to this.

⁵ This can be understood by noting that if $\sum_{\omega} P$ is independent of the integration time (say T), one can write $P \sim 1/T \implies |\tilde{u}_z| \sim 1/\sqrt{T} \implies \sum_{\omega} |\tilde{u}_z| \sim \sqrt{T}$.

$$\mathbf{F}_{\text{kin}} \equiv \langle \rho \mathbf{u}^2 \mathbf{u} / 2 \rangle_{xyt} \quad (18)$$

$$\mathbf{F}_{\text{visc}} \equiv - \langle 2\rho\nu\mathbf{u} \cdot \vec{S} \rangle_{xyt} \quad (19)$$

$$\mathbf{F}_{\text{cool}} \equiv - \hat{z} \int_{z_{\text{bot}}}^z \langle q \rangle_{xyt} dz \quad (20)$$

along with the radiative and SGS fluxes defined in equations 7 and 8. Above, $\langle \square \rangle_{xyt}$ denotes the horizontal and temporal average of \square (in practice, the temporal average is taken over a few turnover times), while q is given by equation 9.

3.6. Diagnostics

We define the Rayleigh number (Ra), which describes the degree of supercriticality of convection, as

$$\text{Ra} \equiv \frac{g |\Delta s| L^3}{C_P \nu \chi} \quad (21)$$

where L is the depth over which the entropy gradient remains negative (i.e. excluding the stably stratified layers at the top and the bottom of the domain); Δs is the integral over this depth of the horizontally and temporally averaged vertical entropy gradient; and χ is the thermal conductivity (in our case, that arising from the Kramers opacity formula, such that $\chi = K_0 \rho^{-3} T^{13/2} C_P^{-1}$). We choose the value of χ corresponding to the midpoint of the region where the entropy gradient is negative. A similar quantity can be defined using the subgrid diffusivity:

$$\text{Ra}_{\text{SGS}} \equiv \frac{g |\Delta s| L^3}{C_P \nu \chi_{\text{SGS}}} \quad (22)$$

We define the Reynolds number, Re, which measures how turbulent the system is, as

$$\text{Re} \equiv \frac{\max_z [u_{\text{rms}}(z)] L}{\nu} \quad (23)$$

The contribution of convection to the total heat transport is characterized by the Nusselt number, Nu, which is the ratio of the total energy flux to that carried by radiation. We also report the peak value of the Mach number:

$$\text{Ma}_{\text{max}} \equiv \sqrt{\max_z [\langle u^2 \rangle_{xyt} / \langle c_s^2 \rangle_{xyt}]} \quad (24)$$

The system can also be characterized by the flux-based Rayleigh Number:

$$\text{Ra}_{\text{F}} \equiv \frac{g l^4 F_{\text{bot}}}{C_P \rho T \nu \chi^2} \quad (25)$$

where ρ , T , and χ are measured at $z = 0$. Note that this is akin to the product of a Rayleigh number and the Nusselt number.

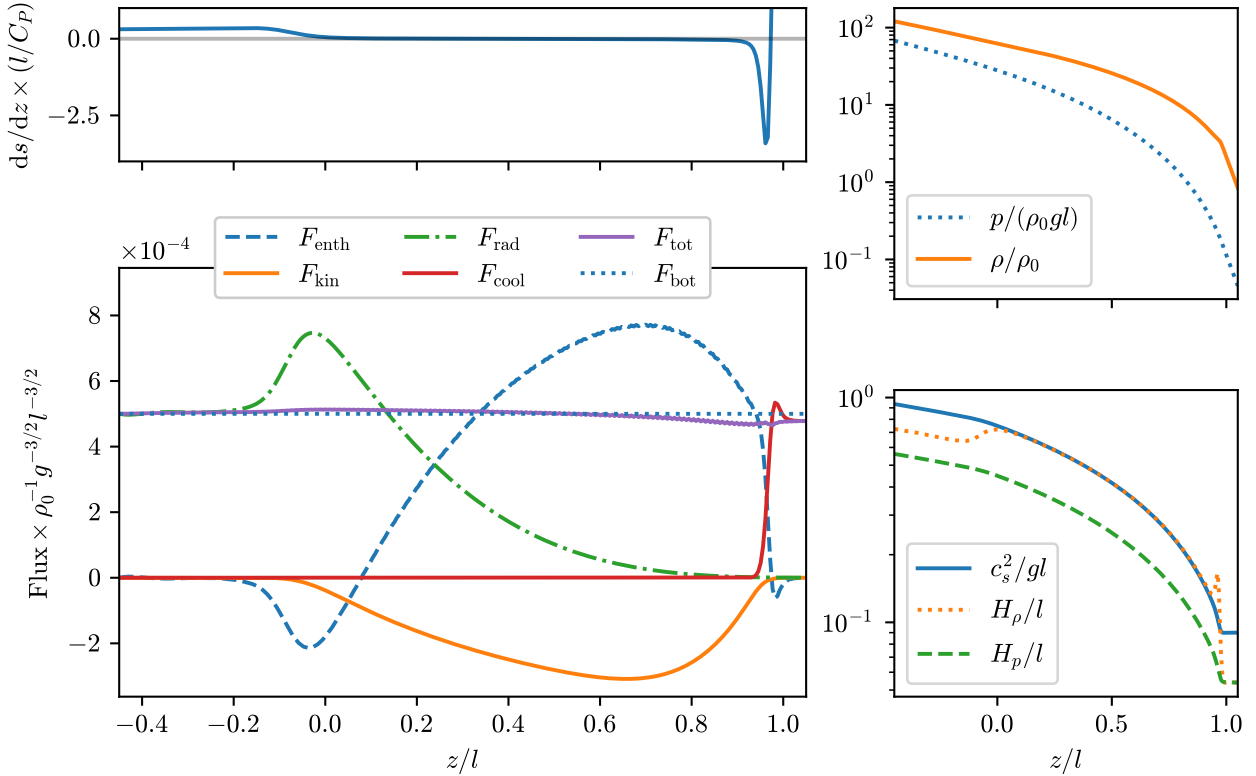


Figure 1. Horizontally and temporally averaged vertical fluxes and other quantities in a realization of the nonmagnetic (NF) simulation. The constant flux marked as F_{bot} is that used to set the boundary condition for the entropy at the bottom of the domain. F_{tot} is the sum of F_{enth} , F_{kin} , F_{rad} , and F_{cool} ; contributions due to F_{SGS} and F_{visc} have not been included.

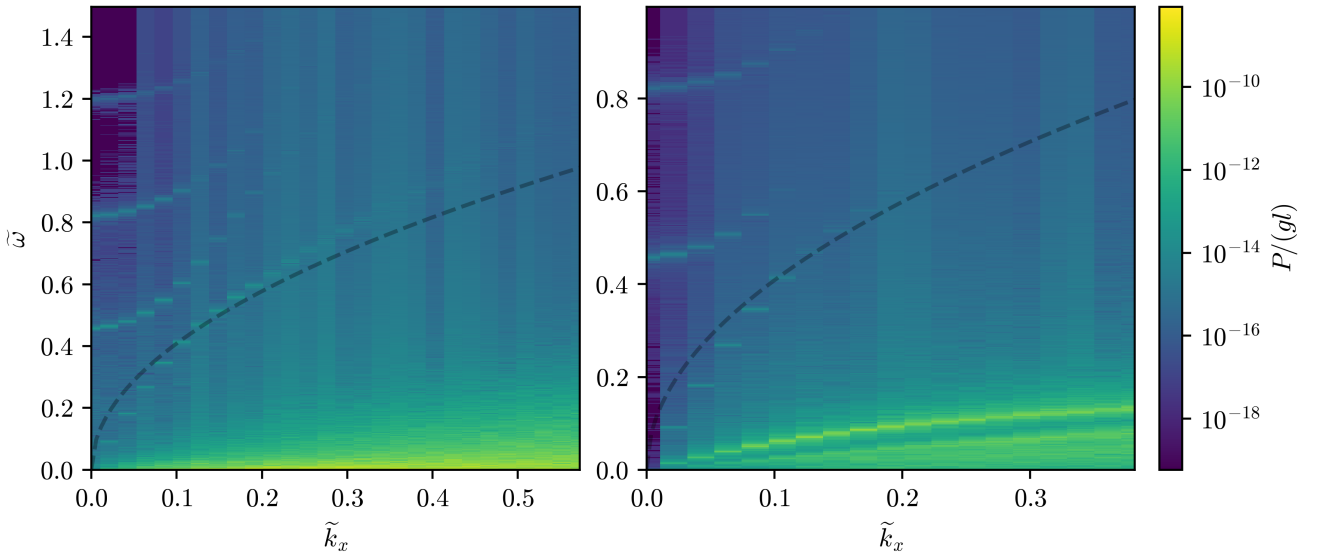


Figure 2. Diagnostic k - ω diagrams generated by averaging over four realizations of the non-magnetic (NF) case for (left) $z = l$; and (right) $z = -0.1l$. In both cases, we have set $\tilde{k}_y = 0$. The dashed black line shows the theoretical dispersion relation of the f mode.

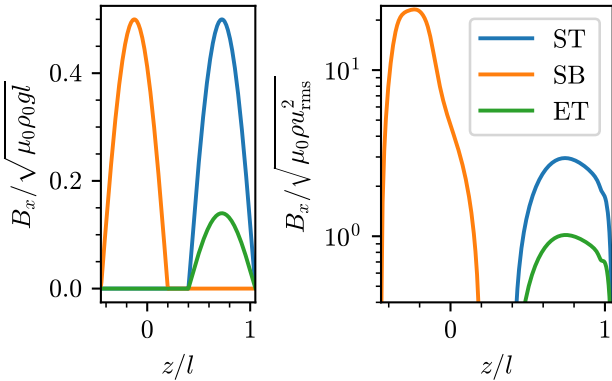


Figure 3. Profiles of B_x in the ST and SB simulations. Recall that the chosen magnetic field is only a function of z . The profiles of ρ and u_{rms} used to normalize the magnetic field correspond to horizontal-temporal averages, just like the quantities shown in figure 1.

4. THE NON-MAGNETIC CASE

Figure 1 shows the vertical components of various fluxes of the energy, along with the density, the squared sound speed, the vertical entropy gradient, and the RMS velocity (all horizontally and temporally averaged) as a function of depth in a single realization of the NF case. The temporal averages have been taken over six turnover times in the statistically steady phase of the simulation. Table 1 lists various diagnostics that characterize the simulation. The stratification becomes stable for $z < 0.36l$, but still remains close to adiabatic for $0 \lesssim z < 0.36l$. Like the Kramers runs discussed by Käpylä et al. (2017), our setup contains an extended Deardorff zone, where the convective flux is positive (directed upward) despite the stratification being stable. Below this is an overshoot zone, where the convective flux becomes negative. The prescribed cooling function leads to almost isothermal stratification for $z > l$, resulting in a steep drop in the density. This density drop is expected to support an f mode.

Figure 2 shows k - ω diagrams at two heights, averaged over four realizations of the NF case. We observe both p and f modes near the top of the domain, while g modes are also visible in the stably stratified overshoot region. The expected dispersion relation of the f mode ($\omega = \sqrt{gk_x}$) has been indicated as a dashed grey line. The deviation of the f mode frequencies from the theoretical curve at high \tilde{k}_x is due to the upper boundary of the domain ($z = 1.05l$) being close to the density jump induced by the cooling layer ($z = l$).

5. STRENGTHENING OF THE F MODE

We now examine how simulations with imposed magnetic fields differ from the non-magnetic case described

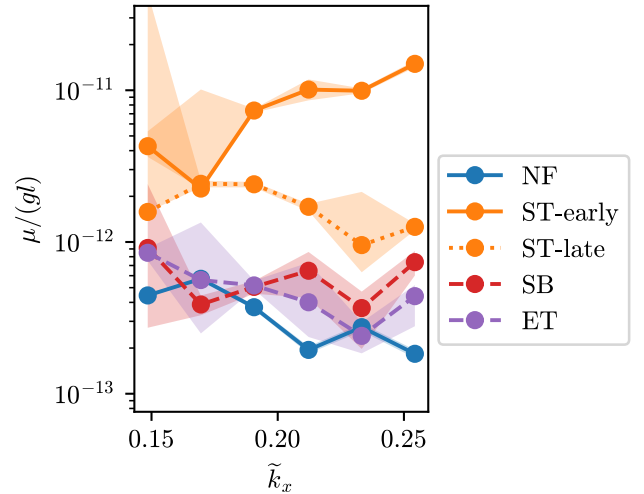


Figure 4. The mass of the f mode at $z = l$ as a function of \tilde{k}_x with $\tilde{k}_y = 0$. The two cases of the ‘ST’ configuration are marked ‘early’ and ‘late’ to indicate the timespan considered (see table 1).

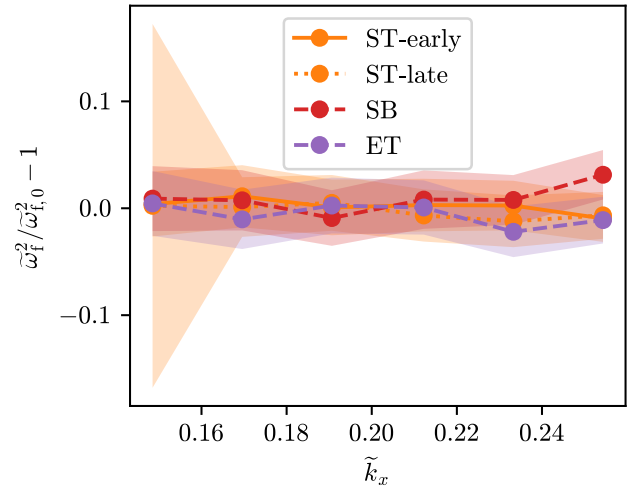


Figure 5. The shift in the frequency of the f mode (with respect to the NF case) at $z = l$ due to the imposed magnetic field, as a function of \tilde{k}_x . The central frequency of the f mode in the magnetic case is $\tilde{\omega}_f$, while that in the non-magnetic case is $\tilde{\omega}_{f,0}$.

above. Table 1 shows the values of various parameters and diagnostics (the latter computed from a single realization) for each configuration.

The different magnetic field configurations are shown in figure 3. Recall that we have chosen magnetic fields such that B_x is the only nonzero component, and it depends only on z . The ST case is around 3.6 times the equipartition value, while the ET case is close to equipartition. In both these cases, the magnetic field is nonzero near the top of the CZ. On the other hand, the

SB case has a magnetic field of the same strength as the ST case, but located below the CZ (and is thus highly super-equipartition). The sensitivity of the f mode at the surface to magnetic fields at different depths can be gauged by comparing the ST and SB cases. On the other hand, the ST and ET cases tell us about the effect of the strength of the magnetic field. While these configurations are simpler than those expected for rising magnetic flux tubes, this study is a preliminary proof of concept.

Recall (section 3.3) that we model the power spectrum at fixed \tilde{k}_x , \tilde{k}_y , and z as the sum of a number of Lorentzians (for the modes) and a power law (for the continuum). Since all the magnetic field configurations we impose do not have any spatial variation in the horizontal direction (unlike the fields one actually expects to find in the Sun), they lead to strong coupling between modes at $\tilde{k}_x = \tilde{k}_y = 0$ and those at nonzero wavenumbers (appendix B). In what follows, we confine ourselves to a range of \tilde{k}_x where the f mode does not seem to be affected by this effect.

Figure 4 shows the mode mass (defined in section 3.4) corresponding to the f mode at $z = l$ as a function of \tilde{k}_x (with $\tilde{k}_y = 0$) for all the magnetic field configurations we consider (along with the non-magnetic case). The mode masses in the SB, ET, and NF cases are not significantly different. On the other hand, the mode masses in the ST case are up to an order of magnitude higher. However, the strengthening of the f mode in the ST case is transient: the mode masses measured immediately after the imposition of the magnetic field (ST-early) are significantly larger than those measured some time later (ST-late).

Figure 5 shows that there is no significant shift in the frequency of the f mode due to imposed magnetic fields. The finiteness of the integration time (which constrains the minimum frequency difference that one can resolve) is the major source of error in the f mode frequencies, and has thus been added in quadrature to the fitting errors for this figure alone. While the lack of a significant shift is at variance with previous forced-turbulence studies that imposed a uniform magnetic field (Singh et al. 2015, fig. 9), it is consistent with studies in which a non-uniform and localized magnetic field was imposed (Singh et al. 2020).

We note that the point where the magnetic field peaks in the SB case is less than 6 pressure scale heights below the point where the f mode is measured. Further, this depth is smaller than the depth over which the eigenfunction of the f mode is expected to decay exponentially (e.g. the eigenfunction of the f mode for $\tilde{k}_x = 0.25$

is expected to decay exponentially over a length scale of approximately $1.36l$).

6. CONCLUSIONS

In agreement with previous forced-turbulence studies (Singh et al. 2020), we have found that a super-equipartition magnetic field localized near the surface causes strengthening of the f mode. On the other hand, an otherwise identical magnetic field centered 6 pressure scale heights below the point of measurement does not seem to affect the amplitude of the f mode. We also find no significant effect for an equipartition magnetic field localized near the surface. None of the magnetic cases shows a significant shift in the frequency of the f mode as compared to the non-magnetic case.

Even in cases where the magnetic field strengthens the f mode, we have found that the strengthening of the f mode is transient, with the mode mass decreasing with time. This means future studies that try to quantitatively constrain solar magnetic fields based on observed mode amplitudes must model both the time evolution and the spatial dependence of these fields.

Quantitative interpretation of observations (Singh et al. 2016; Waidele et al. 2023a) requires a better understanding of how such effects depend on the strength, the spatial scale, and the growth rate of the magnetic field. A more extensive parameter study to this end is in progress. Future work will also examine the effects of magnetic fields on p and g modes in simulations such as those presented here. Similar simulations with rotation may aid the interpretation of observational reports of the cycle-dependence of the power and frequency of solar Rossby modes (Waidele & Zhao 2023).

We thank Matthias Rheinhardt for fixing a bug in Pencil that affected our study. The Gauss Centre for Supercomputing e.V. (www.gauss-centre.eu) supported this project by providing computing time on the GCS Supercomputer SuperMUC-NG at Leibniz Supercomputing Centre (www.lrz.de). We also used the Pegasus HPC facility at IUCAA. We thank Alexandra Elbakyan for facilitating access to scientific literature.

Data Availability: The input files, postprocessing scripts, and a subset of the output (enough to reproduce our results) for all the simulations described in this paper can be downloaded from Zenodo (Kishore et al. 2024). The available output includes horizontally averaged diagnostics and power spectra (the latter at $z = l$ for the magnetic cases, and $z = -0.1l, l$ for the NF cases). Power spectra at other values of z will be provided on reasonable request.

Software: Pencil (Pencil Code Collaboration et al. 2021), SciPy (Virtanen et al. 2020), NumPy (Harris et al.

2020), Matplotlib (Hunter 2007), h5py (Collette et al. 2023), GNU Parallel (Tange 2022).

APPENDIX

A. GRID INDEPENDENCE

To check if the number of grid points is sufficient to resolve all the relevant scales, we consider a set of simulations with $L_x = L_y = 2l$ (all the other parameters are kept identical to those in the NF case). We initialize a simulation with this aspect ratio (keeping the grid resolution unchanged) by tiling a snapshot from the $L_x = L_y = l$ simulation (described in section 2.3) and running it for $300 \sqrt{l/g}$ time units. The resulting snapshot is then linearly interpolated onto grids of different resolutions, keeping the domain size unchanged. These simulations are then run for $500 \sqrt{l/g}$ time units. Various horizontal-temporal averages, calculated by averaging over the last $300 \sqrt{l/g}$ time units, are shown in figure 6. The depicted quantities are converged to within a few percent for $N_z = 288$ (used for the simulations reported in this study).

We note that the mode masses we report are all measured at wavenumbers corresponding to length scales somewhat larger than the integral scale of the convective flows; for reference, a mode with $k = 2\pi/l$ would correspond to $\tilde{k} \approx 0.34$. We thus expect the mode masses to not be more sensitive to the resolution than the quantities shown in figure 6. Figure 7 shows that when the grid spacing is doubled compared to what we have used for our study, the mass of the f mode in the non-magnetic case does not change to an extent that would invalidate our conclusions.

B. MODE COUPLING

Figure 8 shows a k - ω diagram from the ST-early case. Unlike in the non-magnetic case (figure 2), one sees a vertical line at $\tilde{k}_x = 0$. Similar vertical features (referred to as *Bloch modes*) have been observed in earlier work, at multiples of twice the wavenumber of the horizontal variation of the magnetic field (Singh et al. 2014, p. 4; Singh et al. 2020, sec. 3.2). Recall that the magnetic field we have imposed has no spatial variation in the horizontal direction (corresponding to $\tilde{k}_x = \tilde{k}_y = 0$). In simulations where the magnetic field varies sinusoidally in the horizontal direction (not reported here), we also observe such features at twice the corresponding wavenumber. Singh et al. (2020, section 3.3) found that the Bloch modes are absent when the magnetic field is horizontally localized. Since the magnetic fields in sunspots are localized, we do not believe the Bloch modes observed in our setup have any direct observational relevance.

Another difference from the non-magnetic case is the appearance of horizontal bands. These appear to be caused by nonlinear interactions due to the large amplitudes of the p modes at $\tilde{k}_x = 0$. In line with our comments on Bloch modes, we ignore wavenumber ranges where the f mode is affected by this mode coupling.

C. FITTING MODES

The continuum is modelled as a power law,

$$C_1 |\tilde{\omega}|^{-C_2}, \quad (C1)$$

with C_1 and C_2 constrained to be positive. This is motivated by the fact that on dimensional grounds, the frequency spectrum of the turbulent velocity field is expected to scale as $E(\omega) \sim \epsilon \omega^{-2}$, where ϵ is the dissipation rate of the specific kinetic energy.

Each mode is modelled as a Lorentzian,

$$\frac{C_3 \gamma / \pi}{(\tilde{\omega} - \tilde{\omega}_0)^2 + \gamma^2}, \quad (C2)$$

with C_3 constrained to be positive. The half-width at half-maximum (HWHM, γ) is constrained to obey $0 < \gamma < \gamma_{\max}$ with $\gamma_{\max} = 0.05$.

For each value of \tilde{k}_x (recall that we set $\tilde{k}_y = 0$ and $z = l$), $P(\tilde{\omega})$ in the interval $\tilde{\omega}_{\min} < \tilde{\omega} < \tilde{\omega}_{\max}$ is considered (see table 2). The bounds on $\tilde{\omega}$ and the number of modes to be fit are determined by eye and kept fixed. For all the Lorentzians, we require $\tilde{\omega}_{\min} + \gamma_{\max} < \tilde{\omega}_0 < \tilde{\omega}_{\max} - \gamma_{\max}$.

For the non-magnetic case, we consider n_{Lor} Lorentzians with the initial guesses for their frequencies being given by $\tilde{\omega}_{\text{guess}}$ and $\tilde{\omega}_{\text{extra}}$. Due to the effects discussed in appendix B, the magnetic cases have extra peaks of $P(\tilde{\omega})$ as compared to the non-magnetic cases. n_{Lor} and $\tilde{\omega}_{\text{extra}}$ are thus augmented in the magnetic cases by $n_{\text{Lor,mag}}$ and $\tilde{\omega}_{\text{extra,mag}}$ respectively. Table 2 gives the values of these parameters.

To reduce sensitivity to the initial parameter guesses, each mode is fit in two stages. For the first stage, the initial guesses for the mode frequencies are set by eye, and $P(\tilde{\omega})$ is convolved along the frequency axis with a Lorentzian of HWHM 0.01. The considered range of $\tilde{\omega}$ is widened by the same amount. The resulting optimal parameters are then used as initial guesses to fit the unsmoothed $P(\tilde{\omega})$ in the second stage.

For the second stage, the errors in $P(\tilde{\omega})$ (estimated as described in section 2.5) are smoothed along the frequency axis with a top hat of half-width 0.1. During

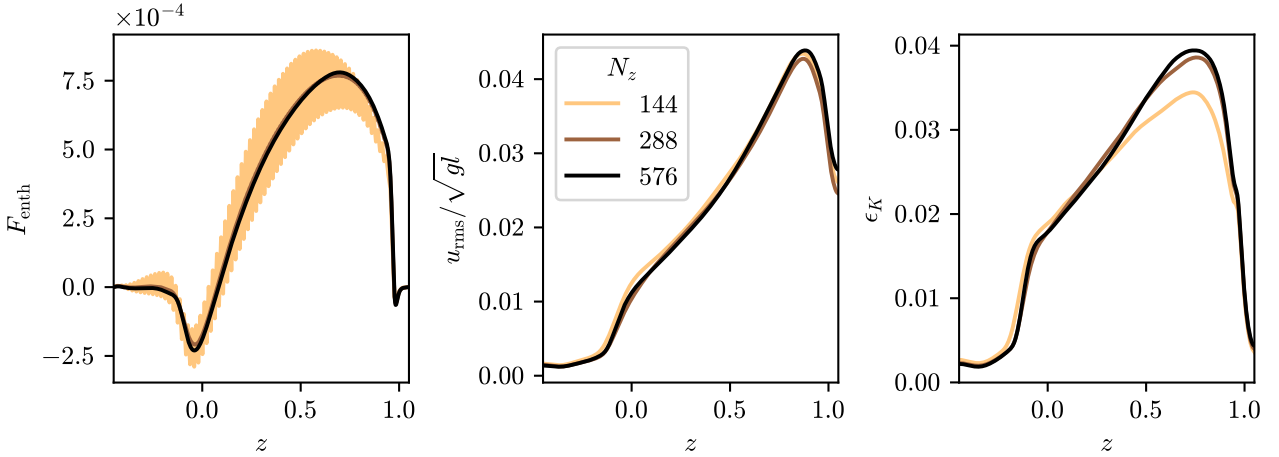


Figure 6. Dependence of various horizontally and temporally averaged quantities on the number of grid points. N_x and N_y are scaled by the same factor as N_z , with only the latter being indicated in the legend. $\epsilon_K \equiv \langle 2\rho\nu S_{ij}S_{ij} \rangle_{xyt}$ is the dissipation rate of the kinetic energy. Note that in the $N_z = 144$ case, F_{enth} oscillates on the grid scale even after horizontal-temporal averaging.

\tilde{k}_x	$\tilde{\omega}_{\min}$	$\tilde{\omega}_{\max}$	$\tilde{\omega}_{\text{guess}}$	n_{Lor}	$\tilde{\omega}_{\text{extra}}$	$n_{\text{Lor,mag}}$	$\tilde{\omega}_{\text{extra,mag}}$
0.15	0.2	0.65	0.52	1		1	0.45
0.17	0.3	0.7	0.55	1		1	0.45
0.19	0.3	1	0.6	2	0.9	2	0.45; 0.82
0.21	0.3	1.3	0.63	3	0.96; 1.15	3	0.45; 0.82; 1.21
0.23	0.3	1.13	0.67	2	1.04	1	0.81
0.25	0.3	1.4	0.72	3	1.08; 1.33	2	0.82; 1.21

Table 2. Parameters used to fit the f mode. Note that all the frequencies listed above are inputs for the fitting routine; these are not the same as the central frequencies of the modes in the final fit.

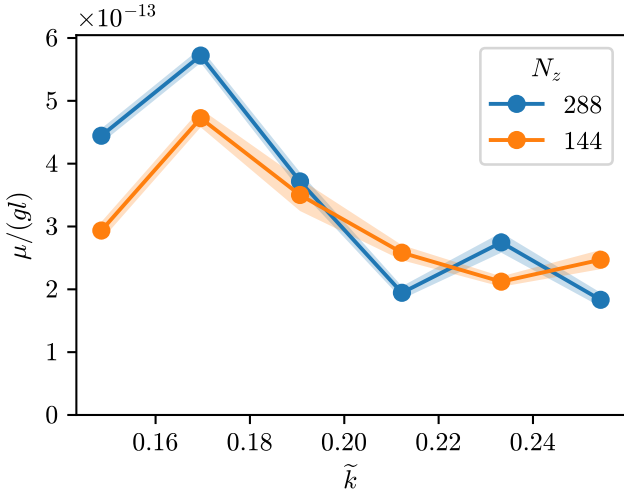


Figure 7. Dependence of the mass of the f mode on the grid resolution. N_x and N_y are scaled by the same factor as N_z , with only the latter being indicated in the legend.

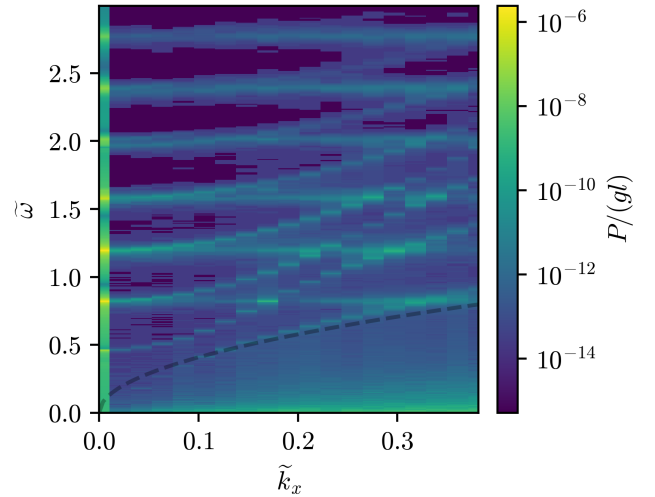


Figure 8. Diagnostic k - ω diagram generated by averaging over all realizations of the ST-early case for $z = l$. In both cases, we have set $k_y = 0$. The dashed black line shows the theoretical dispersion relation of the f mode.

the process of propagating these errors to estimate the

errors in the fit parameters, a scaling factor is applied to the errors in the fit parameters such that the reduced χ^2 of the fit to $P(\omega)$ becomes 1.

Among all the Lorentzians in the final fit, the f mode is identified as the Lorentzian with the largest mass among all the Lorentzians whose central frequency is within 0.05 of $\tilde{\omega}_{\text{guess}}$.

D. ON MODELLING THE CONTINUUM

As discussed in appendix C, we have modelled the continuum (which is expected to be dominated by the spectrum of the turbulent flows themselves) as a power law. The power law slope obtained from our simulations is consistent with the theoretically expected value of 2 (for the different ranges of $\tilde{\omega}$ given in table 2, we find $1.75 \lesssim C_2 \lesssim 2$ for the non-magnetic cases, where C_2 is the negative power law index; the magnetic cases show a larger spread in the power law indices, likely due to

stochastic errors associated with the much smaller time intervals considered).

There seems to be no consensus on what functional form the continuum should take. In previous studies, the continuum was modelled as a polynomial (Singh et al. 2016); as a constant (Singh et al. 2015, 2020); or as the sum of a constant and a Gaussian (Waidele et al. 2023a). Korpi-Lagg et al. (2022) stretched the assumption of a constant background even further, by treating the average of the power spectrum at low frequencies as the continuum at the frequencies of interest.

Recall that Singh et al. (2016) and Waidele et al. (2023a) found that the f mode is strengthened prior to the emergence of active regions. On the other hand, Korpi-Lagg et al. (2022), found no significant strengthening. One possible explanation for this disagreement is the differing treatment of the continuum. Nevertheless, since their analyses differ in other respects too, further study is needed to resolve this issue.

REFERENCES

- Acheson, D. 1990, *Elementary fluid dynamics*, Oxford Applied Mathematics and Computing Science Series (Oxford University Press)
- Anders, E. H., Brown, B. P., & Oishi, J. S. 2018, *Phys. Rev. Fluids*, 3, 083502, doi: [10.1103/PhysRevFluids.3.083502](https://doi.org/10.1103/PhysRevFluids.3.083502)
- Babcock, H. W. 1961, *ApJ*, 133, 572, doi: [10.1086/147060](https://doi.org/10.1086/147060)
- Batchelor, G. K. 1953, *The theory of homogeneous turbulence* (Cambridge university press)
- Bekki, Y., Cameron, R. H., & Gizon, L. 2022, *A&A*, 666, A135, doi: [10.1051/0004-6361/202244150](https://doi.org/10.1051/0004-6361/202244150)
- Blume, C. C., Hindman, B. W., & Matilsky, L. I. 2024, *ApJ*, 966, 29, doi: [10.3847/1538-4357/ad27d1](https://doi.org/10.3847/1538-4357/ad27d1)
- Bracewell, R. N. 2000, *The Fourier Transform and its applications*, 3rd edn. (McGraw-Hill)
- Charbonneau, P. 2020, *Living Reviews in Solar Physics*, 17, 4, doi: [10.1007/s41116-020-00025-6](https://doi.org/10.1007/s41116-020-00025-6)
- Cheung, M. C. M., Rempel, M., Title, A. M., & Schüssler, M. 2010, *The Astrophysical Journal*, 720, 233, doi: [10.1088/0004-637X/720/1/233](https://doi.org/10.1088/0004-637X/720/1/233)
- Christensen-Dalsgaard, J. 2002, *Rev. Mod. Phys.*, 74, 1073–1129, doi: [10.1103/RevModPhys.74.1073](https://doi.org/10.1103/RevModPhys.74.1073)
- Collette, A., Kluyver, T., Caswell, T. A., et al. 2023, *h5py/h5py*: 3.8.0, Zenodo, doi: [10.5281/zenodo.7560547](https://doi.org/10.5281/zenodo.7560547)
- Harris, C. R., Millman, K. J., van der Walt, S. J., et al. 2020, *Nature*, 585, 357–362, doi: [10.1038/s41586-020-2649-2](https://doi.org/10.1038/s41586-020-2649-2)
- Hunter, J. D. 2007, *Computing in Science & Engineering*, 9, 90–95, doi: [10.1109/MCSE.2007.55](https://doi.org/10.1109/MCSE.2007.55)
- Kiefer, R., & Roth, M. 2018, *ApJ*, 854, 74, doi: [10.3847/1538-4357/aaa3f7](https://doi.org/10.3847/1538-4357/aaa3f7)
- Kiefer, R., Schad, A., & Roth, M. 2017, *The Astrophysical Journal*, 846, 162, doi: [10.3847/1538-4357/aa8634](https://doi.org/10.3847/1538-4357/aa8634)
- Kishore, G., Singh, N. K., Käpylä, P., & Roth, M. 2024, Data for ‘Strengthening of the f mode due to subsurface magnetic fields in simulations of convection’, Zenodo, doi: [10.5281/zenodo.13737348](https://doi.org/10.5281/zenodo.13737348)
- Korpi-Lagg, M. J., Korpi-Lagg, A., Olsper, N., & Truong, H. L. 2022, *A&A*, 665, A141, doi: [10.1051/0004-6361/202243979](https://doi.org/10.1051/0004-6361/202243979)
- Käpylä, P. J. 2019, *A&A*, 631, A122, doi: [10.1051/0004-6361/201834921](https://doi.org/10.1051/0004-6361/201834921)
- . 2021, *A&A*, 655, A78, doi: [10.1051/0004-6361/202141337](https://doi.org/10.1051/0004-6361/202141337)
- Käpylä, P. J., Rheinhardt, M., Brandenburg, A., et al. 2017, *The Astrophysical Journal Letters*, 845, L23
- Leibacher, J. W., & Stein, R. F. 1981, in *NASA Special Publication*, ed. S. Jordan, Vol. 450, 263–287
- Miles, A. J., Allen, H. R., & Roberts, B. 1992, *SoPh*, 141, 235–251, doi: [10.1007/BF00155177](https://doi.org/10.1007/BF00155177)
- Parker, E. N. 1975, *ApJ*, 198, 205–209, doi: [10.1086/153593](https://doi.org/10.1086/153593)
- Pencil Code Collaboration, Brandenburg, A., Johansen, A., et al. 2021, *The Journal of Open Source Software*, 6, 2807, doi: [10.21105/joss.02807](https://doi.org/10.21105/joss.02807)
- Rui, N. Z., & Fuller, J. 2023, *Monthly Notices of the Royal Astronomical Society*, 523, 582–602, doi: [10.1093/mnras/stad1424](https://doi.org/10.1093/mnras/stad1424)

- Singh, N. K., Brandenburg, A., Chitre, S. M., & Rheinhardt, M. 2015, *Monthly Notices of the Royal Astronomical Society*, 447, 3708–3722, doi: [10.1093/mnras/stu2540](https://doi.org/10.1093/mnras/stu2540)
- Singh, N. K., Brandenburg, A., & Rheinhardt, M. 2014, *The Astrophysical Journal Letters*, 795, L8, doi: [10.1088/2041-8205/795/1/L8](https://doi.org/10.1088/2041-8205/795/1/L8)
- Singh, N. K., Raichur, H., & Brandenburg, A. 2016, *The Astrophysical Journal*, 832, 120, doi: [10.3847/0004-637X/832/2/120](https://doi.org/10.3847/0004-637X/832/2/120)
- Singh, N. K., Raichur, H., Käpylä, M. J., et al. 2020, *Geophysical & Astrophysical Fluid Dynamics*, 114, 196–212, doi: [10.1080/03091929.2019.1653461](https://doi.org/10.1080/03091929.2019.1653461)
- Tange, O. 2022, GNU Parallel 20220222 (‘Donetsk Luhansk’), Zenodo, doi: [10.5281/zenodo.6213471](https://doi.org/10.5281/zenodo.6213471)
- Thompson, M. J. 2006, *Philosophical Transactions of the Royal Society of London Series A*, 364, 297–311, doi: [10.1098/rsta.2005.1700](https://doi.org/10.1098/rsta.2005.1700)
- Tripathi, B., & Mitra, D. 2022, *The Astrophysical Journal*, 934, 61, doi: [10.3847/1538-4357/ac79b1](https://doi.org/10.3847/1538-4357/ac79b1)
- Virtanen, P., Gommers, R., Oliphant, T. E., et al. 2020, *Nature Methods*, 17, 261–272, doi: [10.1038/s41592-019-0686-2](https://doi.org/10.1038/s41592-019-0686-2)
- Waidele, M., Roth, M., Singh, N., & Käpylä, P. J. 2023a, *SoPh*, 298, 30, doi: [10.1007/s11207-023-02124-7](https://doi.org/10.1007/s11207-023-02124-7)
- Waidele, M., & Zhao, J. 2023, *ApJL*, 954, L26, doi: [10.3847/2041-8213/acefd0](https://doi.org/10.3847/2041-8213/acefd0)
- Waidele, M., Zhao, J., & Kitiashvili, I. N. 2023b, *The Astrophysical Journal*, 949, 99, doi: [10.3847/1538-4357/accae2](https://doi.org/10.3847/1538-4357/accae2)
- Zhao, J., Georgobiani, D., Kosovichev, A. G., et al. 2007, *ApJ*, 659, 848–857, doi: [10.1086/512009](https://doi.org/10.1086/512009)